

Performance predictions and acoustic analysis of the HVAB rotor in hover

Hajar Mali^a, Kawtar Benmansour^b, Omer Elsayed* and Khaoula Qaissi^c

*LERMA Lab., School of Aerospace Engineering, International University of Rabat,
Campus UIR Parc Technopolis, Rocade, Rabat-Sale, 11100 - Sala Al Jadida, Maroc*

(Received April 5, 2022, Revised July 21, 2022, Accepted September 14, 2022)

Abstract. This work presents a numerical investigation of the aerodynamics and aero acoustics of the HVAB rotor in hover conditions. Two fully turbulent models are employed, the one-equation Spalart-Allmaras model and the two-equation $k-\omega$ SST model. Transition effects are investigated as well using the Langtry-Menter $\gamma-Re_{\theta t}$ transition transport model. The noise generation and propagation are being investigated using the Ffows-Williams Hawking model for far-field noise and the broadband model for near-field noise. Comparisons with other numerical solvers and with the PSP rotor test data are presented. The results are presented in terms of thrust and power coefficients, the figure of merit, surface pressure distribution, and Sound pressure level. Velocity, pressure, and vortex structures generated by the rotor are also shown in this work. In addition, this work investigates the contribution of different blade regions to the overall noise levels and emphasizes the importance of considering specific areas for future improvements.

Keywords: CFD simulation, helicopter, hover, HVAB, noise

1. Introduction

Flow-field of the helicopter rotor in hovering flight is characterized by a complicated vortical flow structure. The vortical flow complexity is due to the roll-up and interaction of the rotor blade's tip/root vortices. In addition, the absence of the flow convection phenomenon due to no free stream velocity leads to no-wake transport downwards or away from the rotor region. Hence, higher accuracy and simpler numerical prediction are always sought after. The flow field of a rotor is challenging to predict because of the high vorticity (Hariharan *et al.* 2014). Specifically for helicopters, efforts continue to be made to improve rotor hover predictions (Carnes *et al.* 2019, Jung *et al.* 2014, Mali *et al.* 2022, Zhao *et al.* 2018). A multitude of rotor designs was studied and eventually introduced over the last several decades, such as Sikorsky S-76 rotor (Balch *et al.* 1985), the Pressure Sensitive Paint (PSP) rotor (Wong *et al.* 2018), and the Hover Validation and Acoustic Baseline (HVAB) rotor.

*Corresponding author, Assistant Professor, E-mail: Omer.almatbagi@uir.ac.ma

^aGraduate Student, E-mail: Hajar.mali@uir.ac.ma

^bGraduate Student, E-mail: Kawtar.Benmansour@uir.ac.ma

^cPh.D. Student, E-mail: Khaoula.qaissi@uir.ac.ma

While the PSP rotor has been extensively tested at the 14- by 22-Foot Subsonic Tunnel at the NASA Langley Research Center for aerodynamic characteristics, the HVAB rotor was introduced in 2020 to build a baseline for acoustic validation of helicopter blades among other applications (Overmeyer *et al.* 2020). This rotor configuration is inspired by the planform of the PSP rotor and is characterized by a swept tapered tip. The HVAB rotor was developed in collaboration between the NASA RVLТ Project and the US Army Combat Capabilities Development Command Aviation Missile Center. Presently, the HVAB rotor is scheduled to be experimentally tested at the NASA Ames Research Center. Consequently, the experimental results are not yet released at the moment of this writing.

The HVAB rotor testing aims primarily to provide key data for analysis and validation of rotor aero acoustics and further development of noise mitigation techniques. The main rotor is the principal source of aerodynamic noise on a helicopter (Brentner *et al.* 1994). This noise can be classified into periodic implicit noise and broadband noise. Implicit noise includes thickness and loading noise and noise due to interaction between the blade and the flow around it. Broadband noise is due to turbulence and vortex shedding.

Noise reduction can be achieved by several means. In literature flow control for aerodynamic improvement or noise mitigation for rotor blades is a recurring subject (Elsayed *et al.* 2010, Qaissi *et al.* 2022, Roger *et al.* 2013, Shi *et al.* 2019). Most studies focus on the importance of investigating the flow around the rotor and distinguishing distinct noise sources to design and implement noise reduction techniques.

For a helicopter in a hover, a multitude of challenges is present in predicting the flow behavior (Egolf *et al.* 2017, Weiss *et al.* 2019). Since to maintain a fixed position in the air, the thrust and lift must be balanced with the weight and drag in the absence of the freestream velocity. This added complexity to the flow field and make it difficult to numerically predict the performance of the rotor.

This research considers numerical models for best hover performance and noise prediction and explores key aerodynamic noise sources for a helicopter main rotor in hover conditions. In the absence of experimental data, this work uses low-cost steady and transient simulations and compares the results of different numerical solvers. In addition, critical noise source areas over the PSP-based rotor blade will provide a useful design tool for the intended further noise mitigation technique.

2. Methodology

The flow field around the HVAB rotor is solved using the ANSYS Fluent software. Various turbulence models are investigated for solving the Reynolds Averaged Navier-Stokes (RANS) equations and the Unsteady Reynolds Averaged Navier-Stokes (URANS) equations. For this study, the one-equation Spalart Allmaras model, the two-equation $k-\omega$ SST model, and the Langtry-Menter $\gamma-Re_{\theta t}$ transition transport model was used, and the results are compared.

2.1 HVAB rotor configuration

The HVAB rotor blades are based on the PSP blade planform. The geometrical parameters of the HVAB rotor are summarized in Table 1. The rotor blade is shown in Fig. 1. The blades include three families of airfoils, RC (4)-12, RC (4)-10, and RC (6)-08. These airfoils have a decreasing

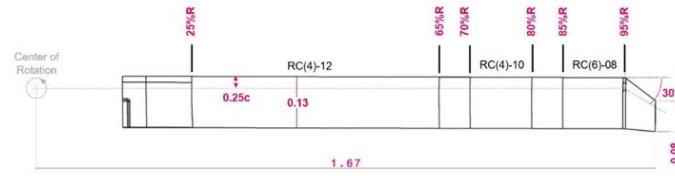


Fig. 1 HVAB rotor blade geometry. Note. Reprinted from “Hover Validation and Acoustic Baseline Blade Set Definition” by Overmeyer and Copp (2020)

Table 1 HVAB rotor properties

Parameters	Value
Number of blades	4
Radius (m)	1.68
Solidity	0.1033
Reference chord (m)	0.138
Tip chord (m)	0.083
Tip Sweep at 95%R	30°
Flap hinge (m)	0.088
Rotor Speed (rpm)	1250.39
Tip Mach Number	0.65

thickness from root to tip. The tip of this blade includes a 30° sweep with a taper which decreases the influence of wave drag and delays the compressibility effects and, thus, improves the rotor performance.

The blades are linearly twisted from root to tip. The highly twisted sections at the root experience lower velocity while the least twisted sections at the tip encounter the highest velocities.

2.2 Grid generation and grid independence

The computational domain, presented in Fig. 2, is a quarter cylinder constructed for a single blade. The remaining rotor blades are accounted for by using appropriate periodic boundary conditions.

An unstructured grid was generated with around 4.9 million cells. The inlet is located 3R above the rotor blade and the outlet 6R below it. A sphere of influence is also implemented around the blade. The blade surface has a structured grid, shown in Fig. 3, made of 86,488 triangular faces. To adequately resolve the boundary layer, a structured grid was generated in the normal direction of the blade surface with a $y^+=1.7$ corresponding to a first-layer thickness of 7×10^{-7} m.

A grid independence study has been conducted to verify that the results are invariant despite the mesh size change. Simulations have been conducted for a different number of elements by making the mesh finer until the obtained results remained constant. A mesh of 4.9 million elements was retained as further refining was unnecessary to the solution. This choice ensured that the results are accurate and time-efficient. Fig. 4 shows the results of the mesh independence investigation. From this graph, we can deduce that above 4.9 million elements, the finer mesh does not improve or impact the results.

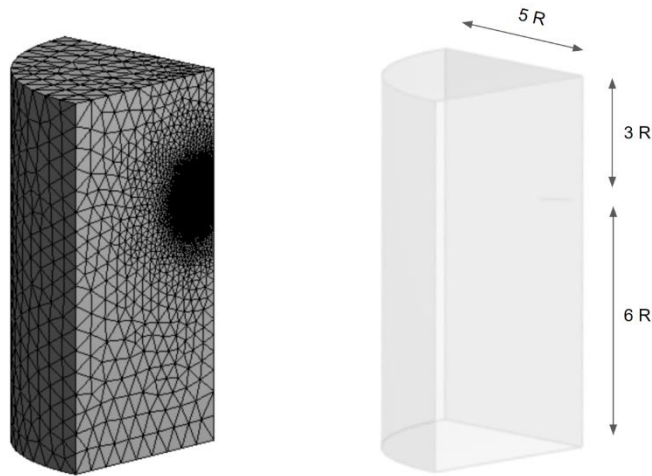


Fig. 2 Blade domain and meshing

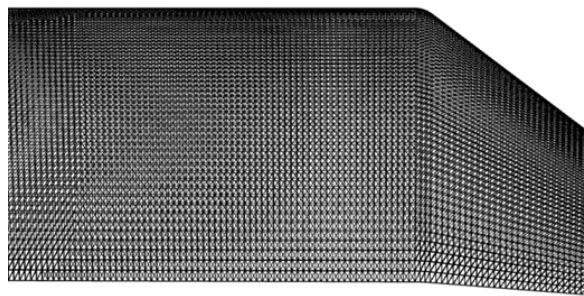


Fig. 3 Blade surface meshing

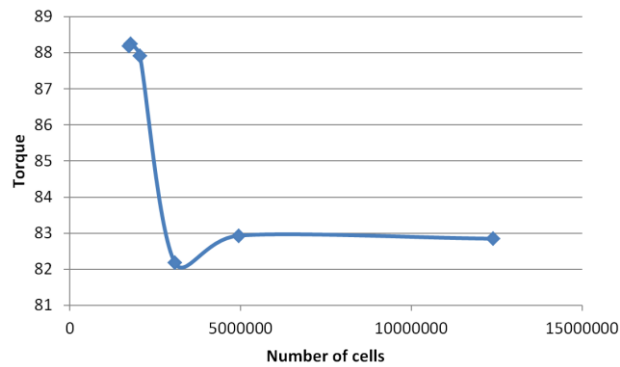


Fig. 4 Torque versus the number of cells for the 6° pitch setting

3. Numerical modeling

3.1 Numerical models

For a Three-dimensional unsteady compressible viscous flow, Eqs. (1)-(2)-(3) represent Navier-

Stokes flow governing equations

$$\frac{\partial(\rho)}{\partial t} + \frac{\partial(\rho u_j)}{\partial x_j} = 0 \quad (1)$$

$$\frac{\partial(\rho u_j)}{\partial t} + \frac{\partial(\rho u_i u_j)}{\partial x_j} = \frac{\partial(\rho)}{\partial x_i} + \frac{\partial(\widehat{\tau}_{ij})}{\partial x_j} + \vec{F} \quad (2)$$

$$\frac{\partial(\rho e)}{\partial t} + \frac{\partial(\rho e u_j)}{\partial x_j} = \frac{\partial(p u_j)}{\partial x_i} + \frac{\partial(u_i \widehat{\tau}_{ij} - q_j)}{\partial x_j} + \vec{F} \quad (3)$$

Where ρ is the density, u_j and u_i are components of the velocity, p is the static pressure, e is the total energy, τ_{ij} and \vec{F} is the stress tensor, the gravitational body force, and external body forces, respectively, and q_j is the rate of total heat flux.

Spalart-Allmaras (SA) model was first used for aerodynamic prediction of the flow over the HVAB rotor. It is a one equation model. It solves the transport equation for ν instead of μ which is the turbulent kinematic viscosity. Since it is a good linear approximation of μ , it offers easier numerical computations. In the SA model, the viscous stress tensor τ_{ij} is related to the Reynolds stresses through the eddy viscosity μ_t , effectively modeling the momentum transfer by turbulent eddies, written in Eq. (4)

$$\tau_{ij} = 2(\mu_l + \mu_t)(s_{ij} - 1/3 \partial u_k / \partial x_k \delta_{ij}) \quad (4)$$

where δ_{ij} is the Kronecker delta and s_{ij} is the strain rate tensor.

To improve the obtained results, the $K-\omega$ SST viscous model is recommended for rotor applications. It has been used by the authors for rotor applications [11 and 16] and has shown good results. The $K-\omega$ SST viscous model is a two equations eddy viscosity model K is the turbulent kinetic energy and ω is the specific turbulent dissipation rate. K and ω are obtained from the transport Eqs. (5)-(6)

$$\frac{\partial}{\partial t}(\rho k) + \frac{\partial}{\partial x_i}(\rho k V_i) = \frac{\partial}{\partial x_j} \left(\Gamma_k \frac{\partial k}{\partial x_j} \right) + G_k - Y_k + S_k \quad (5)$$

$$\frac{\partial}{\partial t}(\rho \omega) + \frac{\partial}{\partial x_i}(\rho \omega V_i) = \frac{\partial}{\partial x_j} \left(\Gamma_\omega \frac{\partial \omega}{\partial x_j} \right) + G_\omega - Y_\omega + S_\omega \quad (6)$$

Where k is the turbulence kinetic energy, ω is the specific turbulence dissipation rate, G_ω is the generation of specific dissipation rate, Γ_k and Γ_ω are the effective diffusivities, Y_k and Y_ω are the dissipation of k and ω and $D\omega$ is the cross-diffusion term.

The transition SST model was also employed to model turbulent flow where a significant part of the boundary layer is laminar. This model couples the two transport equations of the $K-\omega$ SST model with two extra transport equations, therefore, it solves four different equations.

3.2 Noise modeling

The integral formulation of the Ffowcs-Williams Hawking (FW-H) equation allows us to predict aerodynamically generated noise over a rotor. The FW-H equation is a re-arrangement of the flow governing equation and is expressed in Eq. (7)

$$\partial^2 p' = \frac{\partial}{\partial t} [\rho_0 v_n \delta(f)] - \frac{\partial}{\partial x_i} [p n_i \delta(f)] + \frac{\partial^2}{\partial x_i \partial x_j} [H(f) T_{ij}] \quad (7)$$

With $H(f)$ and $\delta(f)$ are the Heaviside and Dirac functions, ρ_0 is the density of the medium, v_n is the local normal velocity, p' is the acoustic pressure, c is the speed of sound and T_{ij} is the Lighthill stress tensor.

Broadband noise modeling is also used. Quantities computable from steady simulations can be used in this method, derived from Lighthill's acoustic analogy, to predict the broadband noise.

4. Results and discussion

The numerical simulation results for the HVAB rotor at different configurations are presented. Since the exact experimental results of this rotor are yet to be released, the results will be evaluated with comparison to available numerical campaigns as well as the closely similar PSP rotor.

4.1 Comparison with PSP rotor experimental data

As mentioned previously, the HVAB rotor design is based on the PSP rotor. The latter has been experimentally tested in the NASA Langley 14×22 Rotor Test Cell and results of the power generation and figure of merits are available in the literature (Lee *et al.* 2019). Because of the similarity between the two rotors, comparisons are made with the existing data of the geometrically identical rotor that is the PSP rotor (Park *et al.* 2020). It is to be noted that the main differences between these two rotors include mass and elastic properties, the hinge location, trailing edge thickness, and tip Mach number.

At low thrust settings, good agreement is detected with PSP measured data for both figures of merit and power predictions. However, at the higher thrust setting, the figure of merit curve starts flattening which is a sign of stall behavior. The power coefficient curve also shows a sharp increase in values. It is to be noted that the HVAB rotor operates at a tip Mach number of 0.65 while the PSP rotor has a tip Mach number equal to 0.58. A higher value of each number leads to a lower figure of merit and lower power consumption at high thrust settings, which agrees with the trend shown in Fig. 5 (a)-(b).

4.2 Turbulence models comparison

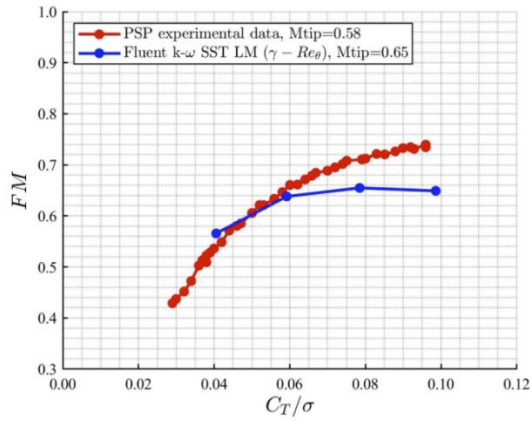
In this study, three different models are used: Spalart-Allmaras model, $k-\omega$ SST model, and Langtry-Menter $\gamma-Re\theta t$ transition model. Fig. 6 presents a comparison of the obtained Coefficient of thrust, the Coefficient of power which is equal to the Coefficient of torque in hover condition, and the Figure of Merit for the turbulence models mentioned previously.

Table 2 presents a comparison of the obtained Coefficient of thrust, the Coefficient of power which is equal to the Coefficient of torque in hover condition, and the Figure of Merit for the turbulence models used. These terms are expressed in Eqs. (8)-(9)-(10)-(11) respectively.

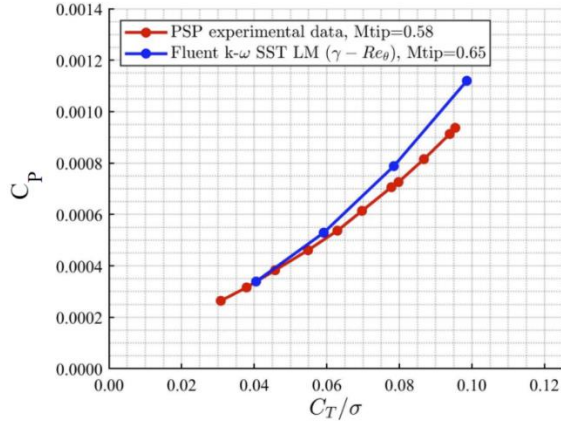
$$C_T = \frac{T}{\rho A (\Omega R)^2} \quad (8)$$

Table 2 Thrust coefficient, power coefficient, torque coefficient, and figure of merit for pitch settings

	6° pitch setting				8° pitch setting			
	CT (10 ⁻³)	CP (10 ⁻³)	CT/σ (10 ⁻²)	FM	CT (10 ⁻³)	CP (10 ⁻³)	CT/σ (10 ⁻²)	FM
Spalart-Allmaras	4.170	0.390	4.036	0.486	6.100	0.572	5.905	0.588
<i>K-ω</i> SST	4.181	0.336	4.046	0.568	6.105	0.527	5.910	0.640
Transition SST	4.186	0.339	4.052	0.565	6.111	0.529	5.916	0.638
	10° pitch setting				12° pitch setting			
	CT (10 ⁻³)	CP (10 ⁻³)	CT/σ (10 ⁻²)	FM	CT (10 ⁻³)	CP (10 ⁻³)	CT/σ (10 ⁻²)	FM
Spalart-Allmaras	8.087	0.839	7.828	0.612	10.170	1.174	9.845	0.617
<i>K-ω</i> SST	8.107	0.786	7.841	0.656	10.172	1.113	9.847	0.652
Transition SST	8.107	0.788	7.848	0.654	10.185	1.120	9.859	0.649



(a) Figure of merit vs torque coefficient



(b) Power coefficient vs torque coefficient

Fig. 5 Results comparison between the HVAB rotor and the PSP rotor

$$C_P = \frac{P}{\rho A (\Omega R)^3} \quad (9)$$

$$C_Q = \frac{Q}{\rho A R (\Omega R)^2} \quad (10)$$

$$FM = \frac{C_T \sqrt{\frac{C_T}{2}}}{C_Q} \quad (11)$$

The simulations are conducted for four different pitch settings: 6°, 8°, 10°, and 12°. The results of the RANS simulation, plotted in Fig. 7, show a close agreement between the *k-ω* SST model and the LM transition model. Although the latter has a set of 4 equations, consisting of the intermittency and the transition onset criterion in terms of momentum thickness Reynolds number equations in addition to those of the *K-ω* model, there isn't a noticeable improvement in the obtained values. Furthermore, the Spalart-Allmaras model is observed to under-estimate or over-estimate randomly the obtained results. This model is not suitable for this application.

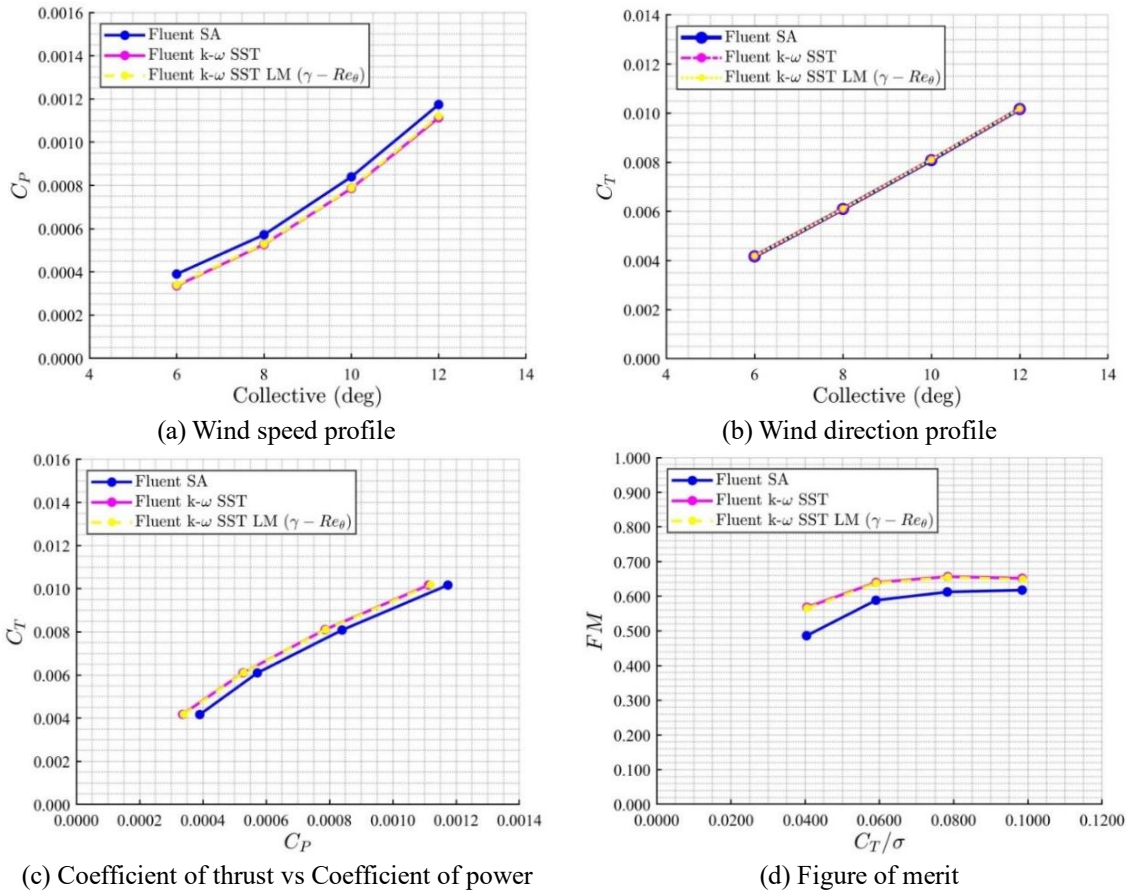


Fig. 6 Results comparison for three turbulent models SA, $k-\omega$ SST and Transient SST

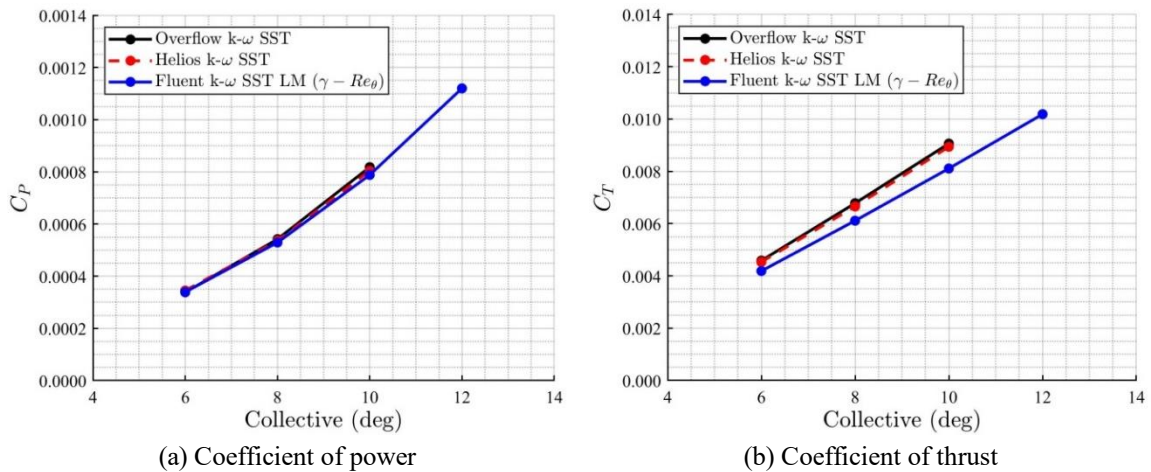


Fig. 7 Results comparison with Overflow and Helios (Narducci *et al.* 2021) for the same HVAB rotor configuration

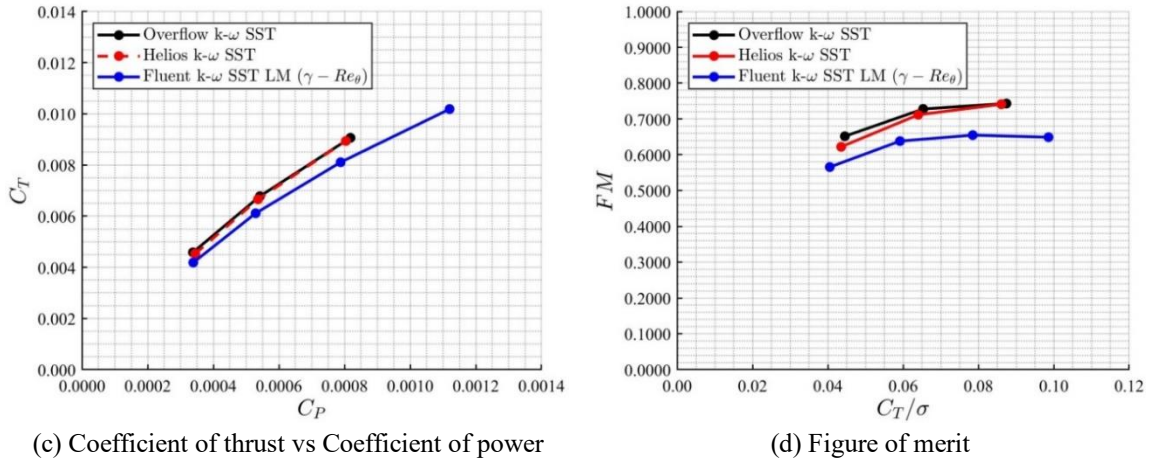


Fig. 7 Continued

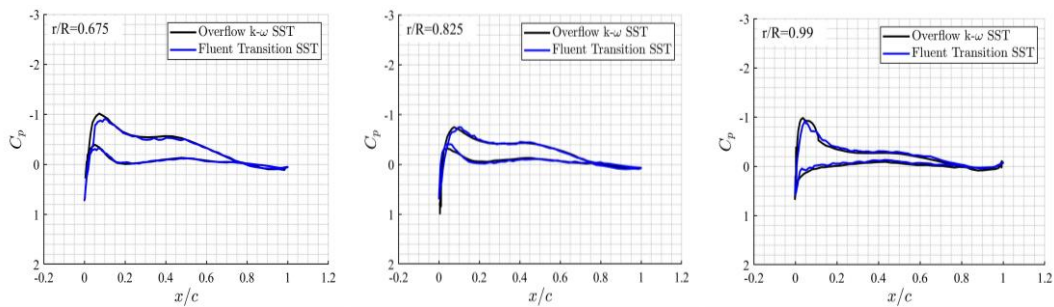


Fig. 8 Pressure coefficient distribution plots at different radial locations (6° pitch setting)

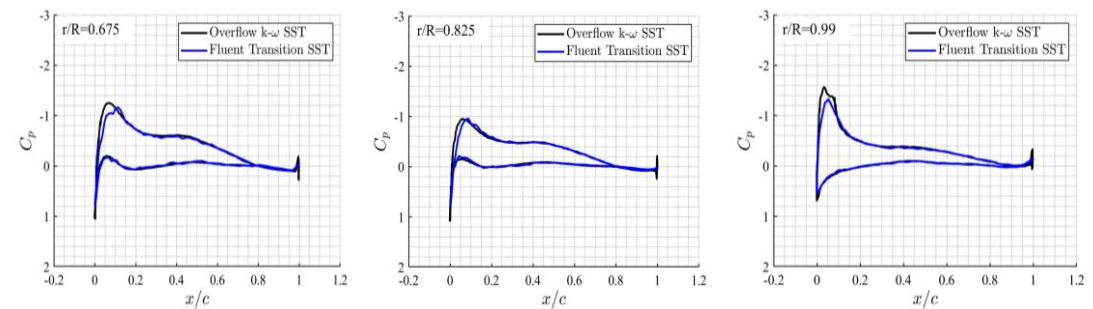


Fig. 9 Pressure coefficient distribution plots at different radial locations (8° pitch setting)

4.3 Aerodynamic loads comparison with OVERFLOW and HELIOS models

A large campaign has been conducted to numerically predict the performance of this rotor for performance assessment prior to experimental testing. This section compares the results obtained using the transition SST model ($k-\omega$ SST LM ($\gamma-Re_{\theta}$) model) with the findings of the OVERFLOW and Helios solvers available in the literature (Narducci *et al.* 2021). The transition SST model is selected as it agreed with the $k-\omega$ SST while taking additional turbulence

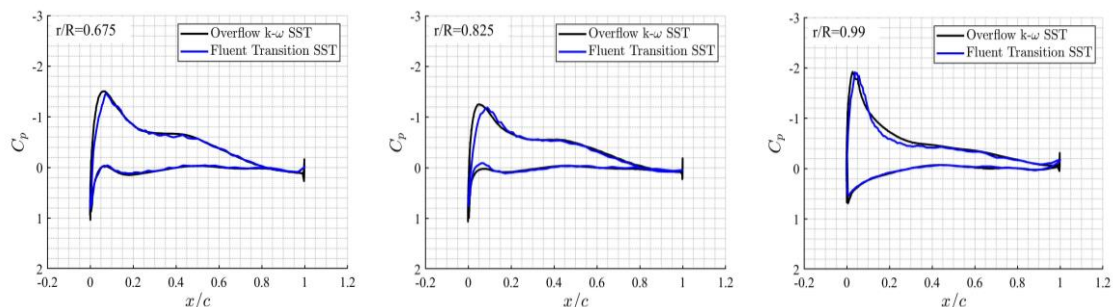
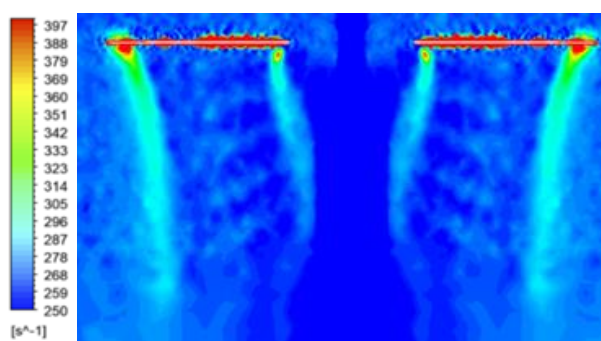
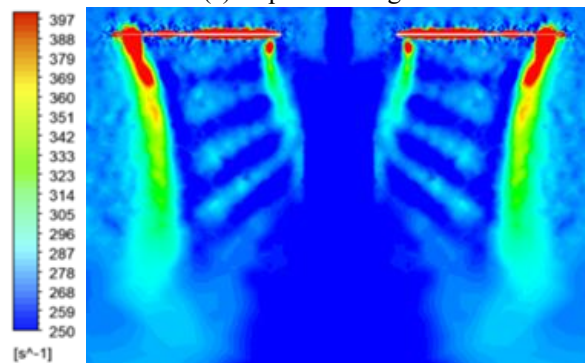


Fig. 10 Pressure coefficient distribution plots at different radial locations (12° pitch setting)



(a) 8° pitch setting



(b) 12° pitch setting

Fig. 11 Rotor vorticity contours

considerations. Fig. 8 details the results of the comparison of the different numerical codes. The power coefficient shows good agreement between all the numerical codes. Meanwhile, the transition SST under-predicts the thrust coefficient compared to OVERFLOW. The figure of merit is also under-estimated, which is expected as it is a function of the thrust coefficient.

Surface pressure distributions are extracted at several radial sections of the rotor blade. The comparison of the transition SST model results with the data of the OVERFLOW solver shows good agreement. Figs. 8-10 show a sample of the pressure distribution at a three radial positions on the blade for three-pitch settings. Surface pressure prediction is crucial for aero acoustics noise sources. The ability of this code to accurately predict the pressure variation at different settings and

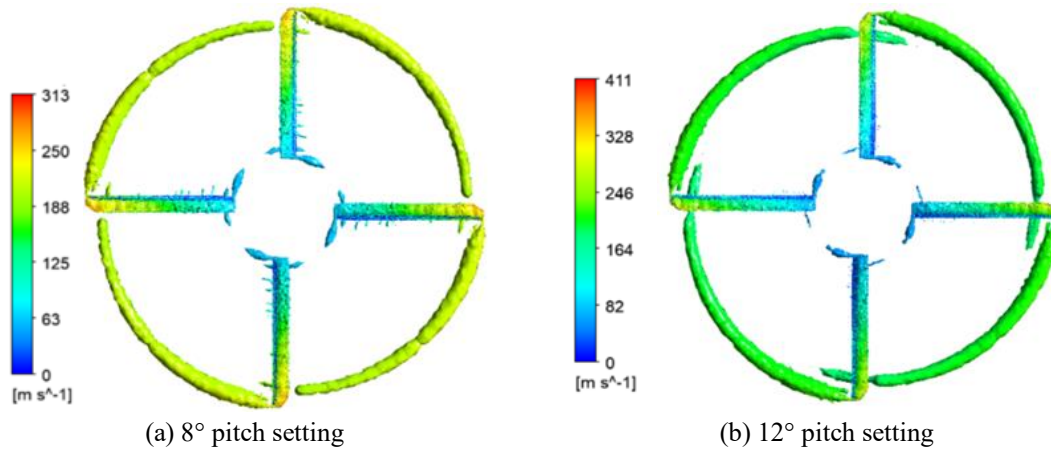


Fig. 12 Vortex core region using Q-criterion method with velocity as the color variable

pitch angles is encouraging.

Q-criterion method at a level of 2.5×10^{-5} . One can first notice how the velocity gets higher from root to tip. Additionally, the vortex structure gets stronger with a larger pitch setting since the flow separation occurs earlier and turbulence gets stronger. The tip velocity calculated from the tip Mach number 0.65 value is 221.17 m/s (725.62 ft/s). The velocity values displayed on the color maps of Fig. 12 show slightly higher velocities due to the high pitch settings used. Overall, the comparison shows satisfactory agreement.

Unlike all the contours presented in this report that used the Transition SST model, Fig. 13 displays a contour in which the LES (Large Eddy Simulation) model is employed at a 12° pitch setting. Transient time was used with an appropriate time step size equal to 0.001s and a maximum of 70 iterations per time step. A coupled scheme was employed with a bounded second-order implicit transient formulation. The rotor geometry and grid specifications remain the same. Unlike RANS (Reynolds Averaged Navier-Stokes) models, the LES model makes it possible to resolve the important unsteady flow structures as well as replicate turbulence within a high level of accuracy. Another major advantage of this methodology is the accurate prediction of recirculated flow and vortex shedding.

This model made it possible to view the contour at different time steps. This figure showcases the vortex core region contour with the Q-criterion method at a level of 2×10^{-5} . The 12° pitch setting case shows a strong tip vortex that extends into the wake of the rotor. The larger pressure difference between the upper and lower surfaces of the blade creates a stronger wake.

5. Acoustic analysis

5.1 Broadband noise sources model

Assessing the acoustics of a rotor allows the visualization of the concentration of noise across the blade to identify the regions of elevated noise emissions to propose and design possible noise mitigation tools. The level of noise generated by the HVAB rotor blade was evaluated by activating the broadband noise source model in the acoustics section of Fluent.

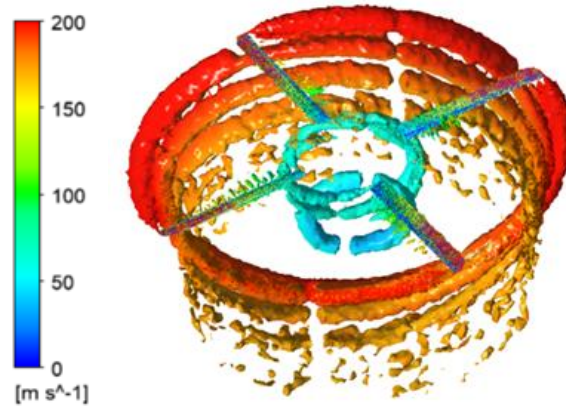


Fig. 13 Vortex core region using Q-criterion method with velocity as the color variable: 12° pitch setting

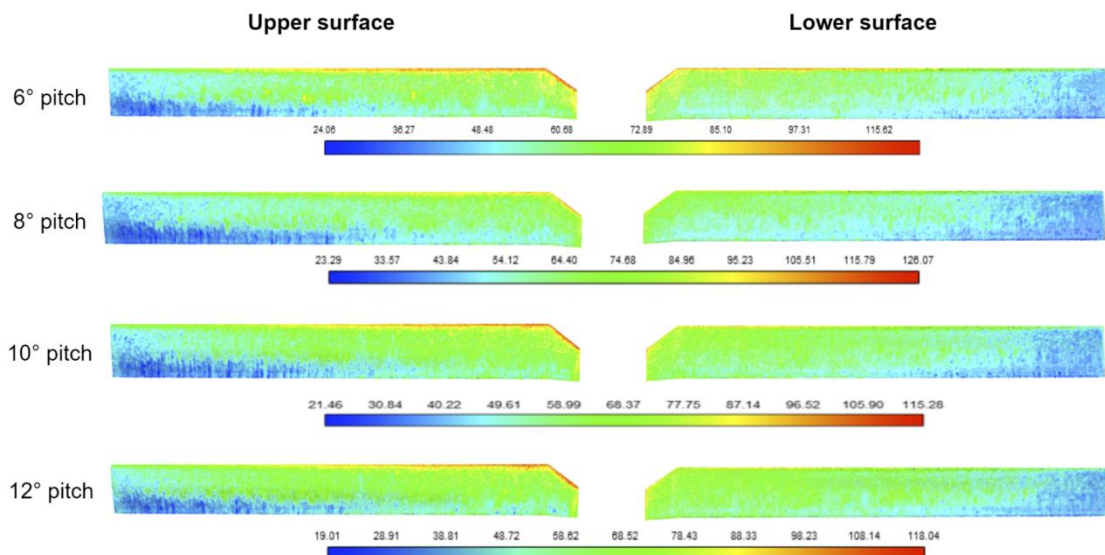


Fig. 14 Surface acoustic power level contours

The surface acoustic power level contours are shown in Fig. 14 for clear visualization of the variation of noise across the blade and to identify the pitch angle at which the noise generation is the lowest and the highest. Higher levels of acoustic power are emitted around the leading edge of the blade near the tip region and lower levels closer to the root. This implies that the highest noise generation occurs towards the tip of the blade due to high tip speed and tip vortex. Based on the color maps below the contours of each pitch setting, the maximum noise is generated at an 8° pitch angle (126.07 dB) while the lowest noise generation is at a 10° pitch angle (115.28 dB). Therefore, we can conclude that the best acoustic performance is provided at the 10° pitch setting.

Fig. 15 presents the percentage of acoustic contribution of each region of the blade. It is shown that more than half of the noise is generated by the leading edge/tip region, which explains the focus of noise mitigation techniques on leading-edge rotor blade areas. Leading-edge serrations for example are highly investigated in the literature.

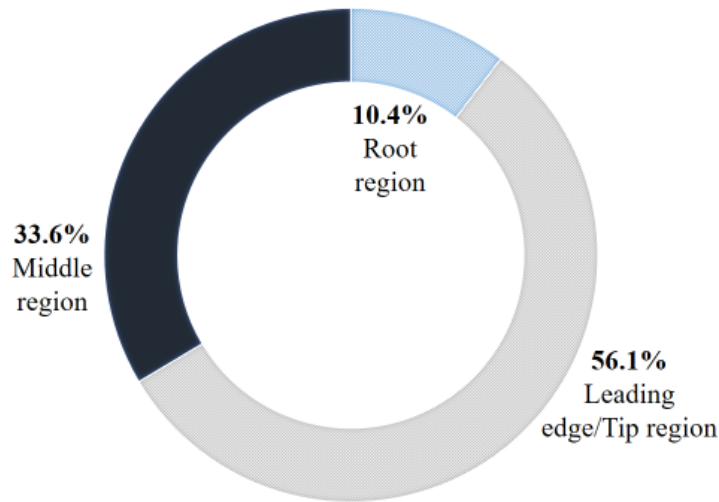


Fig. 15 Acoustic contribution percentage of the rotor blade parts

5.2 Ffowcs Williams and Hawkins model

Unlike the RANS (Reynolds Averaged Navier-Stokes) steady time simulations that were conducted for all the previous results, the LES (Large Eddy Simulation) model with transient time is employed in this section to allow the use of the Ffowcs-Williams and Hawkins acoustic model. An appropriate time step size equal to 0.001s is chosen such that this time step is selected to properly capture the flow even when resolving the smallest cells distance.

After positioning two receivers at different locations behind the trailing edge, a comparison of the sound pressure level peak is made between two pitch angles: 6° and 12° pitch settings. Figs. 16 and 17 show the Sound Pressure Level (SPL) for the two receiver positions in Table 3. It is observed that changing the blade collective angle from 6° to 12° did not result in a significant difference in the maximum SPL values. This matches the finding of (Abrás *et al.* 2021), in which “the rotor blade collective angle did not result in a distinguishable change of the peak SPL values. Therefore, the distance from the blade changes the sound pressure level, however, the variation of the pitch angle does not have a significant impact on the SPL peak value.

5. Conclusions

The hover performance and acoustic emissions of the HVAB rotor with a Mach number of 0.65 are simulated with different turbulence and aero acoustics models. The loads and moments generation are investigated and compared to different numerical codes present in literature as well as the experimental tests of a similar rotor. The noise levels are estimated, and the contribution of the blade parts is included.

The different turbulence models used in this work showed close predictions of the performance of the HVAB. A comparison of the results obtained with ANSYS fluent with numerical codes available in literature shows the ability of this method to accurately predict surface pressure variations. This is important for the acoustic study. However, the simulations under-predicted the

thrust values which results in an under prediction of the figure of merit. The acoustic results illustrated the importance of the leading edge in aerodynamic noise emission. In addition, the sound pressure level showed the effect of receiver position and the pitch angle on the perceived noise level. These results conform to the findings of similar simulations in literature.

Finally, it is important to note that this work is an addition to the large numerical campaigns that led to preparing baseline of predictions for this rotor intended for experimental testing. In the future, the HVAB rotor noise prediction in hover can be compared to the experimental results and re-evaluated to accurately match the tests. This will allow to selection and implement the most appropriate noise reduction techniques.

Data availability

Some or all data, models, or code that support the findings of this study are available from the corresponding author upon reasonable request.

Acknowledgments

Special thanks go to Dr. Lakshmi Sankar at Georgia Institute of Technology and Dr. Po Wei Chen at ANSYS for their constructive feedback and guidance.

References

- Abras, J., Glasby, R., Holst, K. and Hariharan, N. (2021), "Investigation of the impact of deep convergence on the simulation of hovering rotors", *AIAA SciTech Forum*.
- Balch, D.T. and Lombardi, J. (1985), NASA CR 177336, Experimental Study of Main Rotor Tip Geometry and Tail Rotor Interactions in Hover, Vol I-Text and Figures. Retrieved from https://archive.org/details/NASA_NTRS_Archive_19850014034/page/n14
- Brentner, K.S. and Farassat, F. (1994), "Helicopter noise prediction: The current status and future direction", *J. Sound Vib.*, **170**(1), 79-96). <https://doi.org/10.1006/jsvi.1994.1047>.
- Carnes, J.A. and Coder, J.G. (2019), "Computational assessment of the hvab rotor in hover using laminar-turbulent transition modeling", *AIAA Scitech 2019 Forum*, January. <https://doi.org/10.2514/6.2019-0288>.
- Egolf, T.A., Hariharan, N., Narducci, R. and Reed, E. (2017), "AIAA standardized hover simulation: Hover performance prediction status and outstanding issues", *AIAA SciTech Forum-55th AIAA Aerospace Sciences Meeting*, January. <https://doi.org/10.2514/6.2017-1429>.
- Elsayed, O.A., Asrar, W., Omar, A.A. and Kwon, K. (2010), "Influence of differential spoiler settings on the wake vortex characterization and alleviation", *J. Aircraft*, **47**(5), 1728-1738. <https://doi.org/10.2514/1.C000258>.
- Hariharan, N., Egolf, A. and Sankar, L. (2014), "Simulation of rotor in hover: Current state and challenges", *52nd Aerospace Sciences Meeting*, January.
- Jung, M.K., Hwang, J.Y. and Kwon, O.J. (2014), "Assessment of rotor aerodynamic performances in hover using an unstructured mixed method", *52nd Aerospace Sciences Meeting*, January. <https://doi.org/10.2514/6.2014-0042>.
- Lee, B., Jung, Y.S., Jude, D. and Baeder, J.D. (2019), "Turbulent transition prediction of psp hovering rotor using γ - $re\theta$ - sa with crossflow transition model", *AIAA Scitech 2019 Forum*, January. <https://doi.org/10.2514/6.2019-0286>.
- MAlI, H., Banmansour, K., Lakchmi, S. and Chen, P. (2022), "Aerodynamic simulations of the HVAB rotor in

- hover”, *AIAA SciTech Forum*.
- Narducci, R., Jain, R., Abras, J. and Hariharan, N.S. (2021), “HVAB rotor hover computational prediction: A comparative study using OVERFLOW and HPCMP CREATETM-AV Helios”, *AIAA Scitech 2021 Forum*. <https://doi.org/10.2514/6.2021-0617>.
- Overmeyer, A.D., Copp, P.A. and Schaeffler, N.W. (2020), “Hover validation and acoustic baseline blade set definition”, National Aeronautics and Space Administration, Langley Research Center.
- Park, S.H. and Kwon, O.J. (2020), “Numerical study of isolated and full configuration psp rotor using a mixed mesh flow solver”, *AIAA Scitech 2020 Forum*, 1 PartF, January. <https://doi.org/10.2514/6.2020-0529>.
- Qaissi, K., Elsayed, O., Faqir, M. and Essadiqi, E. (2022), “Performance enhancement analysis of a horizontal axis wind turbine by vortex trapping cavity”, *J. Energy Resour. Technol.*, **144**(3), 1-13. <https://doi.org/10.1115/1.4052980>.
- Roger, M., Schram, C. and de Santana, L. (2013), “Reduction of airfoil turbulence-impingement noise by means of leading-edge serrations and/or porous materials”, *19th AIAA/CEAS Aeroacoustics Conference*, 105. <https://doi.org/10.2514/6.2013-2108>.
- Shi, Y., Li, T., He, X., Dong, L. and Xu, G. (2019), “Helicopter rotor thickness noise control using unsteady force excitation”, *Appl. Sci. (Switzerland)*, **9**(7), 1351. <https://doi.org/10.3390/app9071351>.
- Weiss, A., Gardner, A.D., Schwermer, T., Klein, C. and Raffel, M. (2019), “On the effect of rotational forces on rotor blade boundary-layer transition”, *AIAA J.*, **57**(1), 252-266. <https://doi.org/10.2514/1.J057036>.
- Wong, O.D., Watkins, A.N., Goodman, K.Z., Crafton, J., Forlines, A., Goss, L., Gregory, J.W. and Juliano, T.J. (2018), “Blade tip pressure measurements using pressure-sensitive paint”, *J. Am. Helicopt. Soc.*, **63**(1), 1-11. <https://doi.org/10.4050/JAHS.63.012001>.
- Zhao, Q., Wang, J. and Sheng, C. (2018), “Numerical simulations and comparisons of psp and s-76 rotors in hover”, *2018 AIAA Aerospace Sciences Meeting*, 1780. <https://doi.org/10.2514/6.2018-1780>.

EC

Notations

CP	= power coefficient
CQ	= torque coefficient
CT	= thrust coefficient
Cp	= coefficient of pressure
FM	= Figure of Merit
CT/ σ	= blade loading coefficient
A	= rotor radius
R	= rotor radius
ρ	= density
Ω	= Angular velocity
c	= chord length
γ	= intermittency
Re θ t	= transition Reynolds number
k	= turbulent kinetic energy
ω	= specific turbulent dissipation rate